Materials & Design 268 (2026) 116307

Contents lists available at ScienceDirect

Materials & Design

journal homepage: www.elsevier.com/locate/matdes

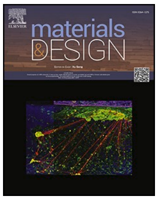

Design of a novel scanning strategy for formation of extremely strong textures in hexagonal materials through laser powder bed fusion

Ryosuke Ozasa [a,b], Yuta Kizawa [a], Kakeru Okawa [a], Koji Hagihara [a,b,c], Kazuhisa Sato [d], Toshiharu Matsumoto [e], Toko Tokunaga [c], Naoko Ikeo [f], Viritpon Srimaneepong [g], Pan Wang [h], Dorte Juul Jensen [i], Takayoshi Nakano [a,b,*]

[a] Division of Materials and Manufacturing Science, Graduate School of Engineering, The University of Osaka, 2-1 Yamadaoka, Suita, Osaka 565-0871, Japan
[b] 3DPTec Integrated Center, The University of Osaka, 2-1 Yamadaoka, Suita, Osaka 565-0871, Japan
[c] Department of Physical Science and Engineering, Nagoya Institute of Technology, Gokiso, Showa-ku, Nagoya, Aichi 466-8555, Japan
[d] Research Center for Ultra-High Voltage Electron Microscopy, The University of Osaka, 7-1 Mihogaoka, Ibaraki 567-0047, Japan
[e] Tobata Seisakusho Co., Ltd., 8-21 Shinsone, Kokuraminami-ku, Kitakyushu, Fukuoka 800-0211, Japan
[f] Department of Mechanical Engineering, Kobe University, 1-1 Rokkodai-cho, Kobe, Hyogo 657-8501, Japan
[g] Department of Prosthodontics, Faculty of Dentistry, Chulalongkorn University, 34 Henri-Dunant Road, Wangmai, Patumwan, Bangkok 10330, Thailand
[h] Singapore Institute of Manufacturing Technology (SIMTech), Agency for Science, Technology and Research (A*STAR), 5 Cleantech Loop, 636732, Republic of Singapore
[i] Department of Civil and Mechanical Engineering, Technical University of Denmark, 2800 Kgs. Lyngby, Denmark

ARTICLE INFO

Keywords:
Laser powder bed fusion
Crystallographic texture
Magnesium
Hexagonal close-packed structure
Crystal growth

ABSTRACT

While crystallographic texture control in cubic metals via laser powder bed fusion (LPBF) has been demonstrated in recent years, achieving such control in hexagonal metals remains a significant challenge. In the present work we present a novel route for the development of a very strong texture in a hexagonal close-packed (hcp)-structured Mg alloy through LPBF. It was achieved by employing reciprocal scanning with a 120° rotation between layers, aligning with the symmetry of Mg's hcp crystal structure. This unique scanning strategy was designed through computational simulation of the heat flux in the melt pool and consideration of the six-fold rotational symmetry along the [0001] axis of the hcp structure. The texture formation was driven by preferential $\langle 11\bar{2}0\rangle$ crystal growth along a direction inclined at approximately 60° to each scanning direction (0°, 120°, and 240°). The LPBF-fabricated specimens showed an anisotropic stress–strain responses in compression test owing to the crystal orientation-dependent selection of operative slip systems, similar to the behavior in a Mg single crystal. These findings highlight the potential in optimizing the scanning strategy by reflecting the symmetry of the crystal structure. This is particularly crucial for LPBF manufacturing non-cubic metals with prominent textures.

1. Introduction

Crystallographic texture control is a crucial approach to induce anisotropic properties in metallic materials such as Goss texture ({110}<001>) formation in electrical steel sheets [1], <100> texture development in β-type Ti alloy for bone implant with low Young's modulus [2], single crystal growth in Ni-based superalloys for turbine blades [3], and so on. Mg alloys, due to their hexagonal close-packed (hcp) structure, also exhibit anisotropic physical properties depending on the crystal orientation, some of which are more pronounced [4] compared to cubic systems. Intrinsic anisotropic properties such as the dissolution behavior for biodegradable implants [5] and mechanical properties [6,7] depend strongly on the texture. Most high-strength structural Mg alloys used in practice have well-controlled crystallographic textures obtained via thermomechanical treatments [8], demonstrating the importance of texture control in Mg alloys. Although single-crystal growth techniques, such as the Bridgman method, can produce relatively large Mg single crystals [9], they are limited in geometric flexibility and processing efficiency.

Laser powder bed fusion (LPBF), as one of the additive

---

* Corresponding author.
E-mail address: nakano@mat.eng.osaka-u.ac.jp (T. Nakano).

https://doi.org/10.1016/j.matdes.2026.116307
Received 16 March 2026; Received in revised form 12 May 2026; Accepted 27 May 2026

manufacturing techniques, provides a feasible approach for fabricating three-dimensional components with arbitrary shapes [10]. Recent studies have reported that LPBF also affects material properties such as strength through solid solution strengthening [11,12] and complex microstructures [13]. Moreover, it has been reported that the crystallographic textures can be tailored by appropriately tuning the process parameters in the LPBF process [14,15]. It should be noted here that the development of strong textures through LPBF has so far only been reported for materials with cubic systems [16]. For example, a single crystalline-like texture was successfully formed through standard scanning strategies (SS) such as a zigzag scanning pattern without interlayer rotation (±0° rotation scanning strategy; ±0°_SS) and with 90° interlayer rotation (±90° rotation scanning strategy; ±90°_SS) [2,14,15].

To the best of our knowledge, the texture in Mg fabricated via different scanning strategies remains unclear and the development of a very strong texture (almost single crystal-like) has not been achieved by LPBF in Mg. Some studies, which employed a zigzag laser scanning pattern with 67° interlayer rotation (±67° rotation scanning strategy; ±67°_SS), obtained a texture with <0001> broadly aligned along the z-axis, while the texture development along the directions perpendicular to z-axis was weak in the WE43 alloy [17–20]. Moreover, ±67°_SS resulted in a polycrystalline structure with a weak texture in TiCN-added AZ91D [21] and Mg-10Gd-3Y-1Zn-0.4Zr alloys [22]. Another study also obtained a polycrystalline structure in the WE43 alloy via ±90°_SS [23]. Such weak textures counteract the potential related to the Mg-specific chemical and mechanical anisotropic properties. Previous studies only focused on Mg alloys containing eutectic phases or compounds that affect crystal growth and the texture formation. Systematic research on relations between scanning strategy and texture development in Mg alloys with few additive elements is needed to establish the methodology for the development of a strong texture in hcp-structured Mg alloys.

With the above-mentioned aim, this study focuses on a Mg-0.5Ca alloy for the following reasons. First, Mg-0.5Ca contains only a minimal amount of solute elements. This compositional simplicity allows to isolate and systematically understand the effect of scanning strategy on texture formation in hcp-structured materials, without significant interference from complex alloying effects such as precipitation or phase transformation. Second, Mg-Ca alloys with a small Ca addition (about 0.5 wt.%) have been widely recognized as promising next-generation biodegradable materials, owing to their well-balanced combination of corrosion behavior and mechanical properties [24,25]. Third, Ca addition effectively increases the ignition temperature of Mg [26,27], thereby improving its flame resistance, which is advantageous for structural applications.

This study investigates the texture formation in Mg-0.5Ca via different scanning strategies with the overarching aim of designing a scanning strategy for the development of a very strong texture. This design is based on the hcp crystal symmetry and the simulation-predicted heat flux direction during solidification. The effectiveness of the designed scanning strategy in controlling the mechanical properties is finally documented.

2. Materials and methods

2.1. Specimen preparation

The Mg-0.5Ca alloy feedstock powder was provided by Tobata Seisakusho (Japan). The average powder particle size was 44.9 µm as measured using a Mastersizer 3000 (Malvern Panalytical, UK). The powder flowability was measured using a Revolution powder analyzer (Mercury Scientific, USA) and showed good flowability, with a rest angle of 35.9° and an avalanche angle of 44.7°. The LPBF process was conducted using the EOS M290 (EOS, Germany) system where the laser power P and scanning speed v were selected within the ranges of 20 to 240 W and 200 to 1000 mm$\cdot$s^{-1}, respectively, while the hatch spacing d, and layer thickness t were 0.06 mm and 0.04 mm. Cubic specimens with dimensions of 5 mm × 5 mm × 5 mm were fabricated in an Ar atmosphere. The density of specimens prepared by ±0°_SS was measured using the Archimedes method. The specimens were mirror polished, and the cross-section was observed through optical microscopy (BX60, Olympus, Japan). The area fraction of the pores on the surface was calculated using ImageJ software (NIH, USA). Through these evaluations, the appropriate fabrication condition (parameter set) for LPBF was determined, as explained in section 3.1. Throughout the LPBF process, the Mg-0.5Ca alloy was safely fabricated without ignition under the conditions applied in this study, demonstrating the effectiveness of the Ca addition as a flame-retardant component to Mg. In this study, the building direction and the direction that runs parallel to the front of the machine were defined as z-axis and x-axis (0° direction) while the y-axis (90° direction) is perpendicular to the x- and z-axes, according to ISO/ASTM 52900 standard terminology.

2.2. Microstructure characterization

The crystallographic textures of the mirror polished specimens were analyzed via an analysis system that combines scanning electron microscopy (JIB-4610F, JEOL, Japan) and electron backscatter diffraction (EBSD; NordlysMax 3, Oxford Instruments, UK), with an accelerating voltage of 20 kV. Inverse pole figure (IPF) maps and pole figures were obtained using Aztec (Oxford Instruments, UK) and processed using Channel 5 (Oxford Instruments, UK). EBSD observations were conducted over an area of 650 × 650 µm^2 with a step size of 2 µm. The uniformity of the crystal orientation was evaluated using multiple uniform distributions (MUDs) [28]. The Schmid factors for possible slip systems and twining system reported in pure Mg [29] were estimated using the EBSD data. First, the Schmid factors of each pixel was calculated as follows:

$$m = cos\varphi cos\lambda \tag{1}$$

where φ is the angle between the loading axis and the slip plane normal, while λ is the angle between the loading axis and the slip direction. The representative Schmid factors were then obtained by averaging the values over all pixels. Here, unlike slip, the formation of $\{10\bar{1}2\}<10\bar{1}1>$ twins exhibit tension-compression asymmetry with respect to the loading axis; therefore, in the calculation of the present compressive deformation, negative values of the Schmid factor (i.e., the Schmid factor for tensile twinning) were regarded as zero. Lattice constants of $a = 0.3220$ nm and $c = 0.5225$ nm, corresponding to a c/a ratio of 1.623, which was obtained using XRD data, were used for calculation. Compared with the lattice constants of pure Mg ($a = 0.3209$ nm, $c = 0.5211$ nm, and $c/a = 1.624$) [30], both the a- and c-axis lattice constants slightly increased, whereas the c/a ratio slightly decreased. These trends are consistent with previous reports [31].

The microstructures of the specimens were examined using scanning transmission electron microscopy (STEM; JEM-ARM200F, JEOL, Japan) equipped with an energy-dispersive X-ray spectrometer (EDS; JED-2300, JEOL, Japan). Specimens for the STEM observations were prepared in the plane perpendicular to z-axis (xy-plane) using focused ion beam (FIB) (Scios2 Dual Beam, Thermo Fisher Scientific, USA).

2.3. Compression test and nanoindentation

The mechanical properties of the specimens were examined using compression tests at room temperature. Rectangular specimens with dimensions of 2 mm × 2 mm × 5 mm were cut from the printed specimens using electro-discharging. The tests were conducted at a nominal strain rate of 1.67 × 10^{-4} s^{-1}, focusing on the dependence of the loading direction relative to the specimen texture. Young's modulus was measured using a nanoindentation system (ENT-1100a, Elionix, Japan) with a Berkovich diamond indenter, where the maximum load was 5 mN. To minimize effects of viscoelasticity on the Young's modulus determination, a hold for 60 s at the maximum load was maintained prior to unloading. The significance of crystal orientation-dependent changes of Young's modulus was tested using a one-way analysis of variance (ANOVA). Post hoc Tukey's honest significant difference was conducted and the statistical significance was set at $p < 0.05$. The SPSS version 25.0 J (SPSS Japan Inc., Japan) was used to perform the statistical analyses.

2.4. Finite-element thermal diffusion simulation

Thermal diffusion simulation was performed using a finite element method (FEM) (COMSOL Multiphysics® 6.4, COMSOL Inc., USA) to investigate the texture formation mechanism as described in detail in [32]. The laser heat sources were modeled using a Gaussian distribution [33] expressed as follows:

$$Q = \frac{4AP}{\pi R^2 H} \exp\left(-\frac{2r^2}{R^2}\right)\left[1 - \frac{z}{H}\right] \qquad (0 < z < H) \tag{2}$$

where Q is the amount of heat per unit volume, A is the laser absorption rate, P is the laser power, R is the laser spot radius (50 μm) [34], r is the distance from the powder bed surface to the center of the laser spot, H is the penetration depth, and z is the depth. The dimensions of the finite element model were 5 mm (width) × 5 mm (depth) × 5 mm (height) and it was divided into a tetrahedral mesh. The heat source was at the center of the top surface and moved along the x-axis. The powder bed was not modeled; however, the energy absorption rate A was set to 65% by comparing the simulated melt pool shape with the actual one [35]. In addition, this study used a surface energy flux absorption model in which the Gaussian heat flux was attenuated with penetration depth from the top surface [36]. Although convection in the melt pool was not calculated in this model, this simplification has a relatively small effect on the melt pool geometry and temperature field [36,37].

The temporal and spatial distributions of the temperature field satisfy three-dimensional heat conduction [38] as follows:

$$\rho C_{\mathrm{p}} \frac{\partial T}{\partial t} + \nabla \bullet \boldsymbol{q} = Q \tag{3}$$

where ρ is the absolute density, C_p is the specific heat capacity, T is the temperature, t is the time, $\boldsymbol{q}$ is the heat flux, and Q is the heat generation amount per unit volume. The initial temperature (T_0) at $t = 0$ was set as the preheating temperature of the baseplate (353 K). The bottom surface of the model was fixed to the initial temperature. The heat flux resulting from heat conduction was expressed by the following equation according to Fourier's law:

$$\boldsymbol{q} = -k\nabla T \tag{4}$$

where k is the thermal conductivity. The boundary conditions on the outer surface of the model were set using the following equation:

$$-\boldsymbol{n} \bullet \boldsymbol{q} = q_0 = h(T_{\mathrm{ext}} - T) \tag{5}$$

where $\boldsymbol{n}$ is the normal vector of the surface, h is the heat transfer coefficient and was set to 10 $\mathrm{W{\cdot}m^{-2}{\cdot}K^{-1}}$, and T_{ext} is the external temperature at which the model contacts the environment (powder bed) and was set to be equal to T_0. The thermophysical properties of Mg-0.5Ca alloy calculated using JMatPro software (Sente Software Ltd., UK) are shown in Table 1. The calculated values show good agreement with previously reported data for pure Mg [39], thereby supporting the validity of the present results. The thermal gradient (G) and solidification rate (R) at each region within the melt pool during solidification were analyzed.

Table 1
Physical and thermophysical parameters of Mg-0.5Ca alloy used in the thermal diffusion simulation.

Physical parameters	Unit	Mg-0.5Ca
Density	$\mathrm{g \cdot cm^{-3}}$	1.740
Thermal conductivity	$\mathrm{W \cdot m^{-1} \cdot K^{-1}}$	153
Specific heat	$\mathrm{J \cdot kg^{-1} \cdot K^{-1}}$	1023
Latent heat of fusion	$\mathrm{kJ \cdot kg^{-1}}$	340.7
Solidus temperature	K	791
Liquidus temperature	K	920

3. Results

3.1. Appropriate process parameter of LPBF

In order to determine appropriate process parameter for the Mg-0.5Ca alloy, a first set of specimens were manufactured via ±0°_SS by varying the laser power and scanning speed. Fig. 1 shows the Archimedes density results. The density of the specimens tended to increase with increasing the laser energy density (ED). From these results, the appropriate process parameter for obtaining the LPBF-fabricated product was selected to be $P = 120$ W, $v = 400$ $\mathrm{mm \cdot s^{-1}}$, $d = 0.06$ mm, and $t = 0.04$ mm (resultant ED = 125 $\mathrm{J \cdot mm^{-3}}$, see red point in Fig. 1). This specimen has a relatively high Archimedes density of ~1.72 $\mathrm{g \cdot cm^{-3}}$ with well-defined shape control, and a surface relative density of 99.8% based on the ImageJ analysis.

3.2. Local thermal conditions

The local thermal conditions are important in the formation of the microstructure and texture during the solidification process; the thermal gradient and solidification rate are generally accepted to be related with the morphologies of the crystal grains while the heat flux direction influences the preferential growth direction of the grains [40]. Thus, understanding thermal conditions is crucial when designing scanning strategies for optimal microstructure and texture. In this study, a single-track thermal diffusion simulation was performed. Fig. 2 shows the solidification conditions at the solid/liquid interface for each region in the melt pool (Fig. 2(a)) and a G-R plot (Fig. 2(b)). For Mg alloys, the Hunt's columnar-to-equiaxed transition (CET) criterion has been reported only for the Mg–3Al alloy [41]. Therefore, in the present study, the criterion of Mg–3Al was employed to predict the grain morphology of the present Mg-0.5Ca alloy. As the solidification conditions of Mg-0.5Ca alloy exceeded the CET criterion, the formation of columnar grains is expected in all areas inside the melt pool, which is required for obtaining a strong texture. Fig. 3(a) presents the temperature distribution at the uppermost xy-plane, and Fig. 3(b-d) shows the resulting melt pool shape and heat flux directions in the yz-, xz-, and xy-planes. As shown in Fig. 3(a, d), the melt pool exhibits a circle-like morphology when observed in the xy-plane, and the tail of the melt pool is extremely short. Furthermore, the results of the simulation shown in Fig. 3(b, c) demonstrate that the

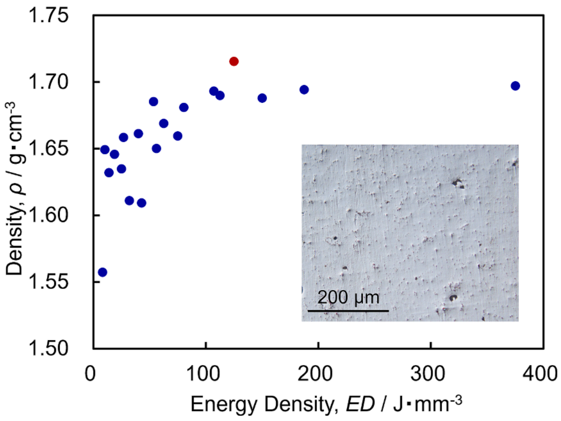

Fig. 1. Archimedes density of the specimens manufactured by ±0°_SS as a function of the laser energy density. Inset is an optical micrograph from the yz-plane of the specimen marked by a red dot, which showed the highest density.

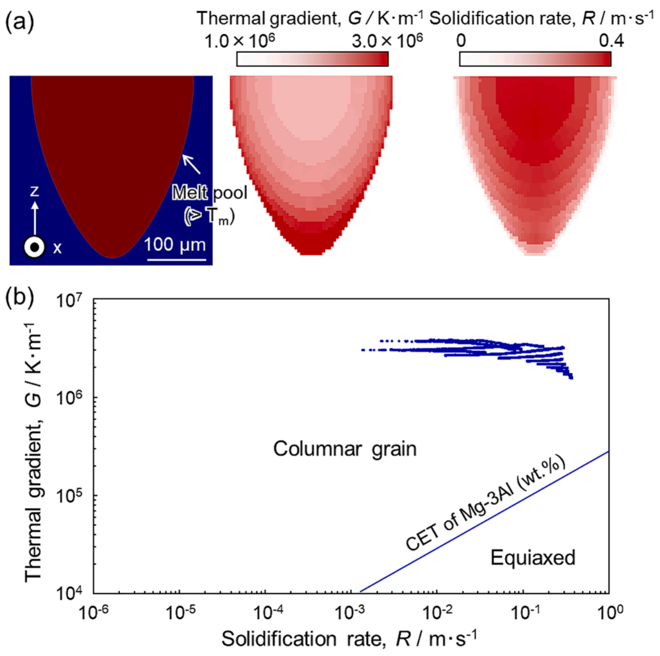

Fig. 2. Solidification condition in Mg-0.5Ca alloy calculated by single-track thermal diffusion simulations. (a) Distribution of the thermal gradient (G) and solidification rate (R) at the solid/liquid interface in the melt pool and (b) the predicted G-R plots with the Hunt's columnar-to-equiaxed transition (CET) criterion for Mg-3Al (wt.%) alloy [41].

melt pool exhibits a spindle-shaped morphology in three dimensions and that the heat flux along z-axis is barely observable. Note that in the xy-plane, the heat flux is aligned perpendicularly to the tangent line of the tail of the melt pool (Fig. 3(d)), indicating that the shape of the tail determines the heat flux direction. Fig. 3(e) shows the angle of the heat flux direction ($|\theta|$) against the scanning direction as a function of the distance from the tail end of the melt pool measured in the xy-plane. To determine the preferential direction of heat flux in the xy-plane, the ratio of the regions where heat flux is aligned along $\theta \pm 10^\circ$ to the total tail regions of the melt pool was analyzed as follows:

$$\text{Regional ratio} = \left(x_{(|\theta|+10^\circ)} - x_{(|\theta|-10^\circ)}\right)/x_{90^\circ} \times 100\ [\%] \tag{6}$$

The simulated result shown in Fig. 3(f) demonstrates that the heat flux in the melt pool occurred most preferentially at approximately ±60°. The present simulation thus predicts that the preferential growth direction of Mg alloys, that is $<11\overline{2}0>$ [42], grow along ±60°-inclined axis relative to the laser scanning direction in the xy-plane.

3.3. Scanning strategy design

Based on the simulation-predicted heat flux direction inclined at ±60° to each laser scanning direction, together with the hcp crystal symmetry, a zigzag laser scanning pattern with a 120° rotation interlayer rotation (±120° rotation scanning strategy; ±120°_SS) was designed to achieve a very strong texture. Specifically, reciprocal laser scanning is performed along the 0°/180°-axes in the (3n-2)$^{\text{th}}$ layer, 120°/300°-axes in the (3n-1)$^{\text{th}}$ layer, and 240°/60°-axes in the (3n)$^{\text{th}}$ layer with an interlayer rotation angle of 120°. Fig. 4 schematically illustrates this proposed novel scanning strategy and the predicted direction of crystal growth. The black arrows indicate the laser scanning directions. With that scanning strategy, we expected that grains will grow with the $<11\overline{2}0>$ direction along the 60°/300°-directions followed by the outward scanning along the 0°-axis and the 120°/240°-directions followed by the return scanning along the 180°-axis in the (3n-2)$^{\text{th}}$ layer, the 60°/180°-directions followed by the outward scanning along the 120°-axis and the 0°/240°-directions followed by the return scanning along the 300°-axis in the (3n-1)$^{\text{th}}$ layer, and the 180°/300°-directions followed by the outward scanning along the 240°-axis and the 0°/120°-directions followed by the return scanning along the 60°-axis in the (3n)$^{\text{th}}$ layer. Thus, the reciprocal scanning along the three scanning directions (0°/180°, 120°/300°, and 240°/60° axes) in each layer should enable $<11\overline{2}0>$ growth from six different directions (0°, 60°, 120°, 180°, 240°, 300°, and 360°), which correspond to the symmetry of the $<11\overline{2}0>$ axes on the (0001) basal plane, *i.e.*, it is

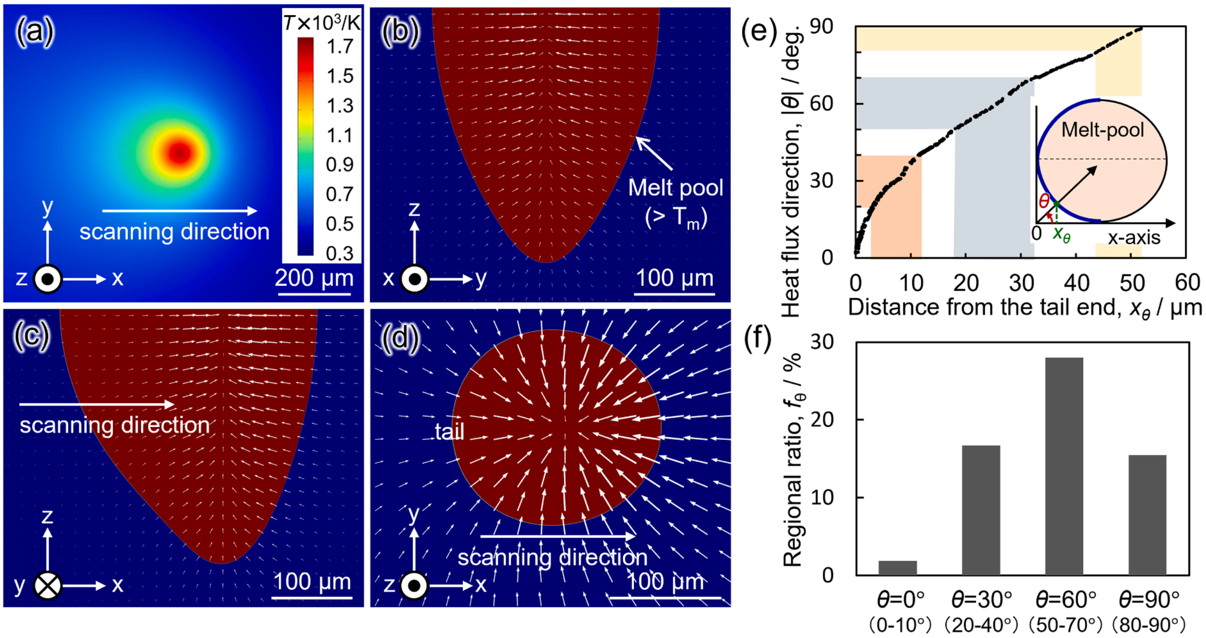

Fig. 3. Directional temperature field simulated using the single-track model. (a) Temperature distribution viewed from the top of the melt pool as well as melt pool geometries and heat flux distributions in the (b) yz-, (c) xz-, and (d) xy-planes. The small white arrows indicate the inverse direction of the heat flux. (e) Angle of heat flux direction as a function of distance from the tail end (x_θ), and (f) regional ratio of the preferential direction of heat flux (f_θ) along 0°, 30°, 60°, and 90° about x-axis.

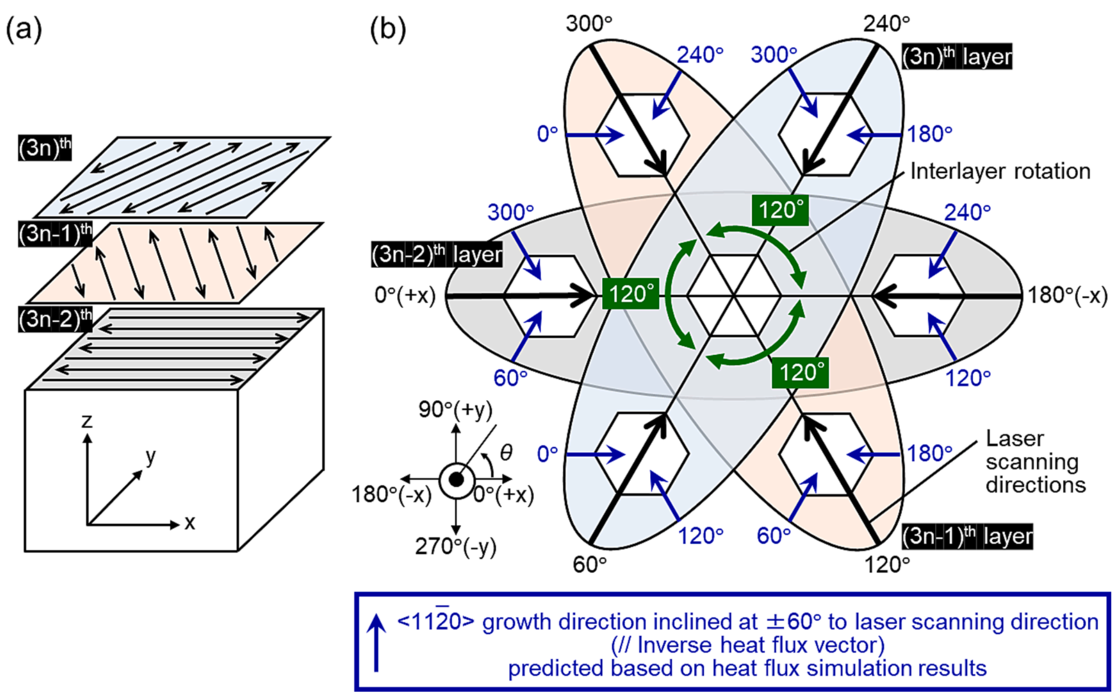

Fig. 4. Schematics of the ±120°_SS and the simulation-predicted crystal growth directions. (a) The reciprocal scanning with an interlayer rotation angle of 120° (±120°_SS). Arrows indicate laser scanning directions. (b) The simulation-based prediction of $\langle 11\bar{2}0\rangle$ growth from six different directions (0°, 60°, 120°, 180°, 240°, 300°, and 360°) followed by each laser scanning along the ± 0° (0° and 180°) in the (3n-2)$^{\text{th}}$ layer, ±120° (120° and 300°) in the (3n-1)$^{\text{th}}$ layer, and ± 240° (240° and 60°) in the (3n)$^{\text{th}}$ layer, viewed from the z-axis. Black and blue arrows indicate the scanning directions and preferential crystal growth directions during the ± 120°_SS process, respectively. White hexagons schematically indicate the hexagonal crystal lattice. n is a natural number.

consistent with six-fold rotational symmetry along the [0001] axis. The effect of this scanning strategy is further explained and discussed in section 4.2.

3.4. *Crystallographic texture and microstructures*

To investigate the effects of scanning strategy on texture and test the validity of the proposed ±120°_SS, this study fabricated a series of specimens using the laser parameter set determined from the data shown in Fig. 1 employing ±120°_SS as well as standard scanning strategies of ±0°_SS and ±90°_SS. Fig. 5 shows IPF maps representing crystal orientation. The ±120°_SS clearly resulted in the development of a single-crystal-like texture, in which z-axis was parallel to $\langle 0001\rangle$, and the x-axis and y-axis are parallel to $\langle 11\bar{2}0\rangle$ and $\langle 10\bar{1}0\rangle$, respectively (Fig. 5(a)). In contrast, in the case of ±0°_SS (Fig. 5(b)) and ±90°_SS (Fig. 5(c)), the formation of a basal-fiber texture was detected, in which only $\langle 0001\rangle$ is preferentially aligned almost parallel to z-axis. This texture in the specimens printed by ±0°_SS and ±90°_SS is similar to that of previously reported in the WE43 alloy [17–20,43]. The effects of the different scanning strategies are clearly seen by the distribution of orientation angles of each crystal orientation against the coordinate axes in each specimen (Fig. 5(d)). Table 2 summarizes the indicators used to evaluate the degree of crystal orientation. These results quantitatively verify the formation of a single-crystal-like texture via ±120°_SS. To the best of our knowledge, this is the first report on the development of a single-crystal-like texture in hcp-structured Mg alloys.

Fig. 6(a, b) shows SEM images of the microstructure within the xy-plane of the ±120°_SS specimen. The images reveal that the elongated microstructures and grain boundaries follow a zigzag pattern in each track at an angle of approximately 60° to the scanning direction. At the melt pool center where the solidification fronts migrated from both the right and left sides of the melt-pool along the ±60°-inclined axis, fusion boundaries having some degrees of misorientation were formed as indicated by the light blue broken lines in Fig. 6(b). Fig. 6(c) displays the orientation map and $\langle 11\bar{2}0\rangle$ pole figures measured at points A–C, which shows that the alignment direction of the zigzag morphology of the microstructures corresponded to $\langle 11\bar{2}0\rangle$. These results suggest that in the ±120°_SS specimen, the grains growth, with $\langle 11\bar{2}0\rangle$ along the direction inclined at approximately 60° to the scanning direction, occurred in the two-dimensional xy-plane, resulting in the very strong texture. To further confirm the preferential growth direction of $\langle 11\bar{2}0\rangle$ grains, the microstructure in the yz-plane at the top layer of the specimen was also observed as shown in Fig. 6(d). The grain boundaries in the melt pool were found to be elongated almost parallel to the top surface. This supports the assumption by the simulation (Fig. 3) that the two-dimensional growth of $\langle 11\bar{2}0\rangle$ grains occurred in the xy-plane. Furthermore, bright field STEM observation (Fig. 6(e)) revealed that the dislocation cells are formed parallel to the grain boundaries and their size is ~1 μm. Based on STEM-EDS observation (Fig. 6(f)), it was found that most of the Ca was homogeneously dissolved in the Mg matrix, while few nanosized Ca precipitates were formed both at grain boundaries and grain interiors. Approximately 0.2 wt.% of Ca is in the Mg matrix, which exceeds the solubility limit of ~0.1 wt.% [44].

3.5. *Mechanical properties*

Nanoindentation and compression tests were performed for the single-crystal-like textured ±120°_SS specimen and the basal-fiber textured ±0°_SS specimen. Fig. 7 shows the Young’s modulus measured along different loading axis. Despite the different textures in the specimens, the measured Young's moduli are comparable. The Young’s modulus along $\langle 0001\rangle$ z-axis is only slightly higher in the ±120°_SS specimens (44.0±2.3 GPa; Fig. 7(a)) compared to the ±0°_SS specimens (41.8±2.4 GPa; Fig. 7(b)).

While the elastic responses of the two specimens are almost similar, the plastic deformation behavior varies significantly depending on the textures. Fig. 8(a) shows the compressive stress–strain curves of the ±120°_SS specimen measured with the loading axis along different

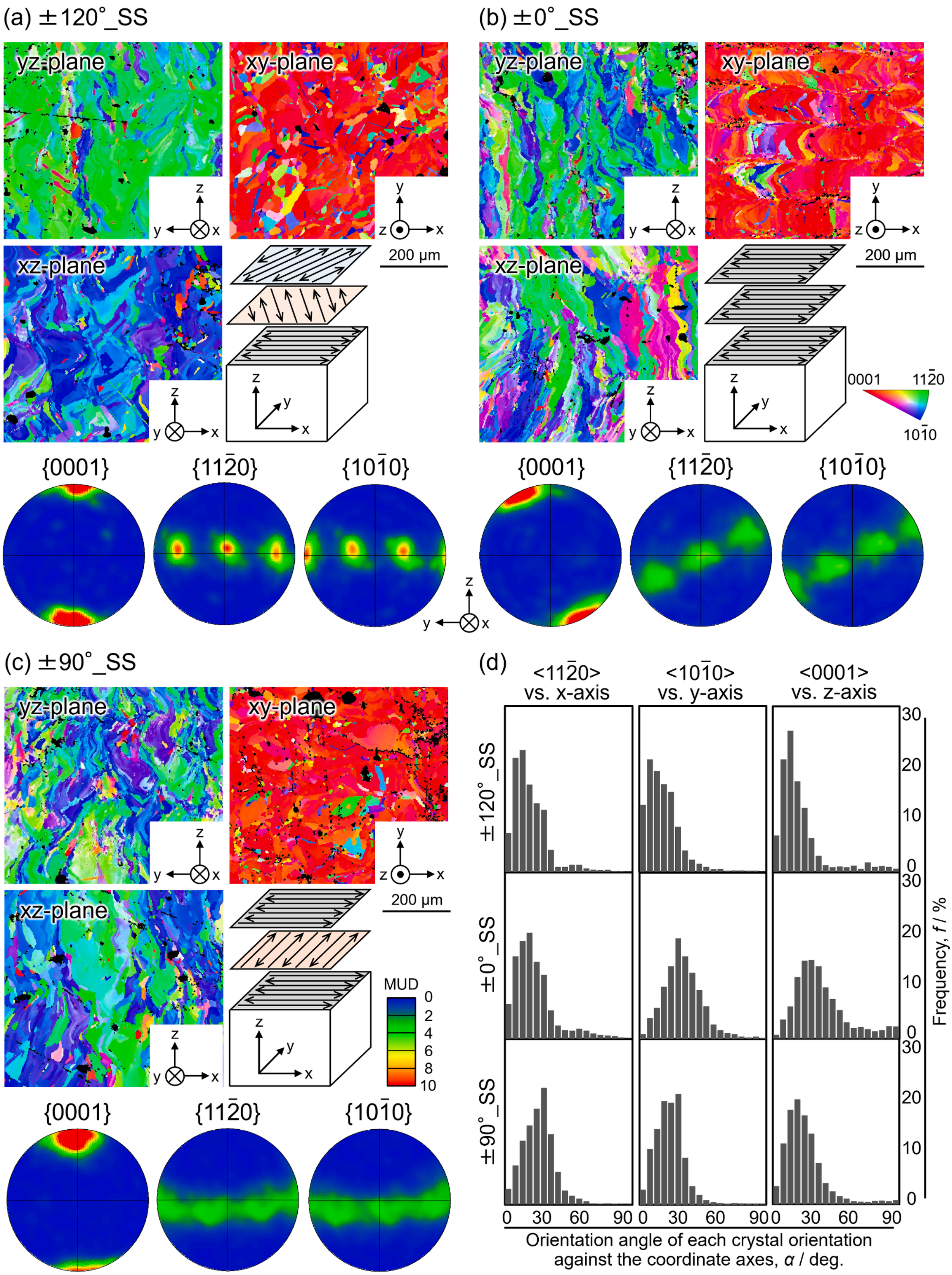

Fig. 5. Textures developed via different scanning strategies. IPF maps measured on the yz-, xz-, and xy-planes, and the corresponding {0001}, $\{11\bar{2}0\}$ and $\{10\bar{1}0\}$ pole figures measured on the yz-plane, obtained from specimens fabricated by (a) the ±120°_SS, (b) the ±0°_SS, and (c) the ±90°_SS. In the figures, the scanning strategies are graphically illustrated for better understanding. (d) Distribution of the orientation angle of each crystal orientation against the coordinate axes in each specimen.

Table 2

Indicators describing the degree of crystal orientation. $f_{<hkil>grains}$ is the frequency of <hkil>-oriented grains within 15° of each coordinate axis. $MUD_{\{hkil\}}$ represents the orientation density of a particular crystal plane normalized by the orientation density of a random texture.

Indicators	±0°_SS	±90°_SS	±120°_SS
$f_{<0001>grains//z}$ [%]	10.0	31.5	52.6
$f_{<11\bar{2}0>grains//x}$ [%]	38.8	21.6	49.8
$f_{<10\bar{1}0>grains//y}$ [%]	10.2	26.6	50.7
$MUD_{\{0001\}}$ [a.u.]	18.2	21.6	26.9
$MUD_{\{11\bar{2}0\}}$ [a.u.]	4.9	4.3	11.9

specimen axis. Assuming a perfect single crystal, loading axes of 0°, 45°, and 90° to the z-axis tilting along the x-axis, i.e. tilting along the <11$\bar{2}$0> zone axis, correspond to <0001>, <$\bar{1}$101.07>, and <$\bar{1}$100>, respectively. Similarly, loading axes of 45° and 90° from z-axis, tilting along the y-axis, i.e. tilting along the <$\bar{1}$100> zone axis corresponds to <11$\bar{2}$1.85> and <11$\bar{2}$0>, respectively. For the ±120°_SS specimens, the yield stress (shown as bar graphs in Fig. 8(a)) and fracture strain (shown as points in Fig. 8(b)) differs significantly depending on the loading direction relative to the crystal orientation: the yield stress along <0001> z-axis is 2.7 times higher than that along <$\bar{1}$101.07> 45°(y)-axis. The stress-strain curve at <11$\bar{2}$1.85> 45°(x)-axis showed an almost similar profile to that at <$\bar{1}$101.07> 45°(y)-axis and the yield stress along these axes (45°) was much lower than that of the <0001> z-axis. In contrast, the fracture strain along <$\bar{1}$101.07> and <11$\bar{2}$1.85> is 2.6 times larger than that along <0001> z-axis. The stress−strain behaviors of the <10$\bar{1}$0> y-axis and <11$\bar{2}$0> x-axis are comparable and both the yield stress and fracture strain showed intermediate values. These results clearly show significant mechanical anisotropy in the ±120°_SS specimens, resembling that of perfect single-crystals [45–47].

The anisotropy of the plastic deformation behavior of the ±0°_SS specimens was also examined by selecting the geometrically identical loading axes. As expected, the ±0°_SS specimens exhibit less mechanical anisotropy (Fig. 8(c)) due to their broad and inclined fiber-texture, compared to the ±120°_SS specimens. The yield stress along z-axis is not significantly higher than the yield stresses along the other loading axes. Instead, the 45°(y)-axis shows the highest value in yield stress and the lowest fracture strain, as shown in Fig. 8(d). The yield stress along the 45°(y)-axis is 1.6 times larger than that along the 45°(x)-axis and fracture strain along the 45°(x)-axis is 2.1 times larger than that along the 45°(y)-axis.

4. Discussion

In this study, we investigated effects of scanning strategy on texture formation and showed that we could develop a very strong, single-crystal-like texture in a hcp-structured Mg alloy using a novel LPBF scanning strategy with ±120°_SS, designed based on the direction of heat flux generated by laser irradiation and the unique six-fold rotational symmetry along the [0001] axis of hcp structure.

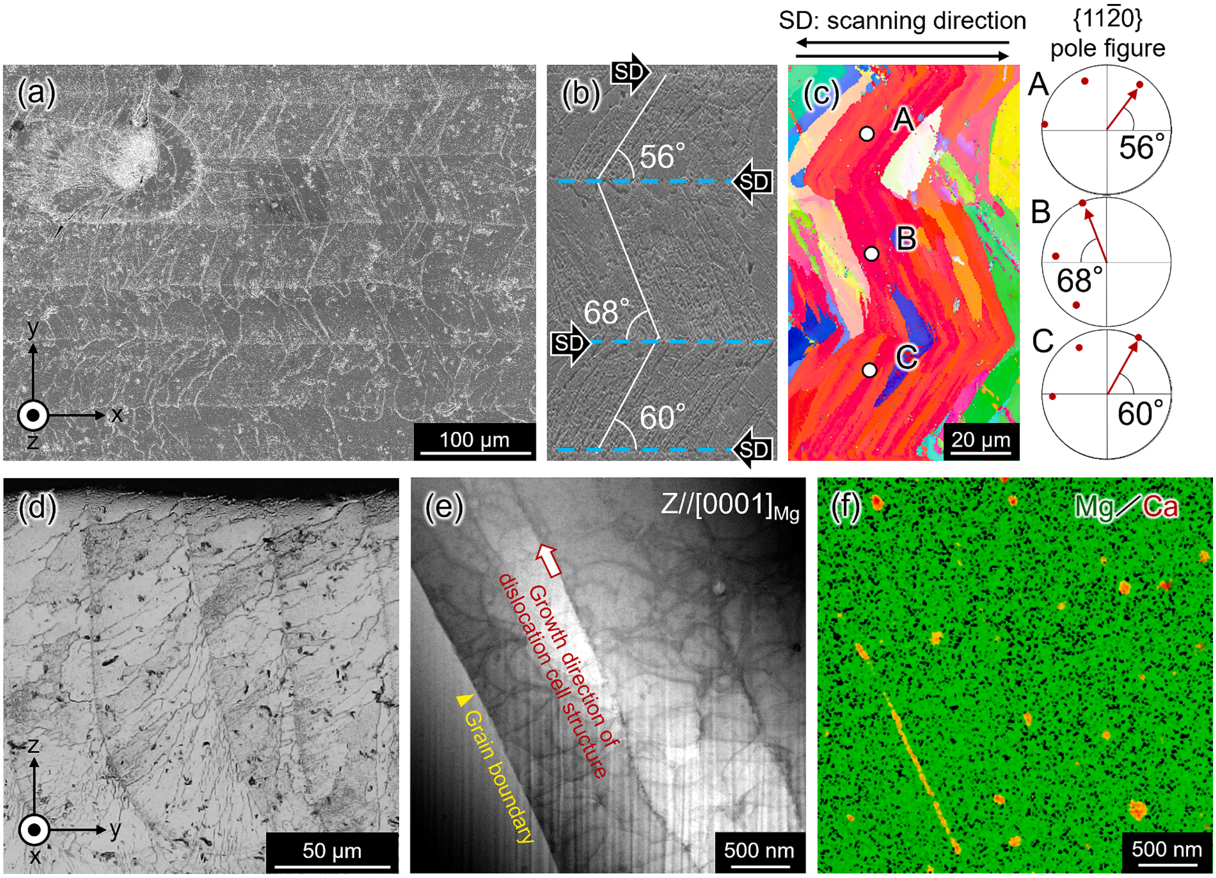

Fig. 6. Microstructural observations of ±120°_SS specimen. SEM images with (a) low magnification and (b) high magnification (where light blue broken lines represent fusion boundaries) and the corresponding (c) IPF map with pole figures measured at points A-C. (d) SEM image at the top layer of the specimen observed on the yz-plane perpendicular to x-axis (laser scanning direction in this layer). (e) Bright field STEM image and the corresponding (f) STEM-EDS elemental map, observed on the xy-plane perpendicular to z-axis.

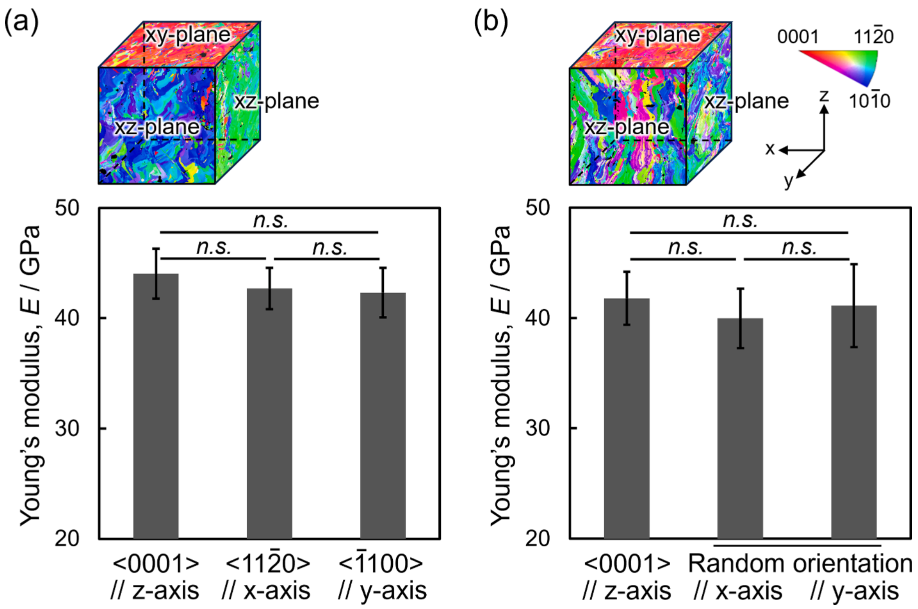

Fig. 7. Young's modulus in each crystal orientation in the (a) ±120°_SS and (b) ±0°_SS specimens. The data (n = 5) were averaged and shown as mean ± standard deviation (SD). *n.s.*: no significant difference.

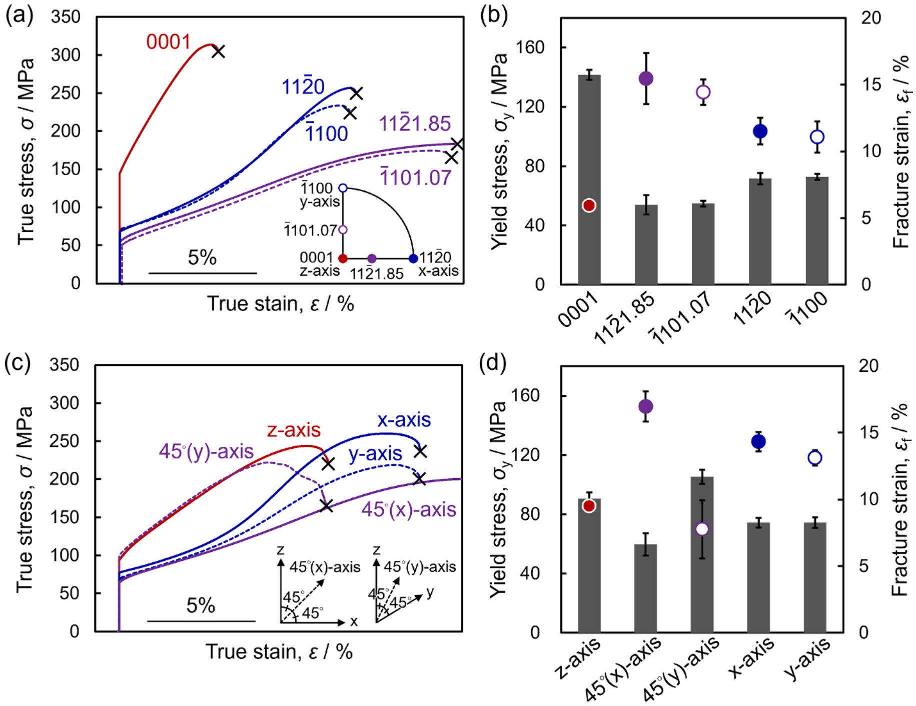

Fig. 8. Crystal orientation dependance of compressive mechanical properties. True stress-true plastic strain curve of the (a) ±120°_SS and (c) ±0°_SS specimens. Measured yield stress and fracture strain of the (b) ±120°_SS and (d) ±0°_SS specimens. Bar graphs and points represent yield stress and fracture strain, respectively in (b) and (d).

4.1. Comparison of thermal diffusion behavior in Mg-0.5Ca alloy and β-type Ti alloy

This study revealed that the solidification behavior in the Mg-0.5Ca alloy where the two-dimensional growth of the <11$\bar{2}$0>-oriented crystal grains occurred in the “xy-plane” (Fig. 3 and Fig. 6) is completely different from that observed in materials with cubic system. Previous studies focusing on the Ti-15Mo-5Zr-3Al (wt.%) alloy, a β-type Ti alloy with body-centered cubic (bcc) structure, reported that the grains with <100> grow within the plane perpendicular to the laser scanning direction, that is the yz-plane when laser scanning along x-axis, and developed a strong texture by the standard ±0°_SS and ±90°_SS in LPBF [14,15]. The difference in the solidification directions of Mg-0.5Ca alloy and Ti-15Mo-5Zr-3Al alloy is related to the difference in the melt-pool shape and the resulting heat flux distribution. The ratio of the length of the tail to melting depth for the Mg-0.5Ca alloy (Fig. 3(b), 3(c)) is calculated to be 0.86 compared to 7.2 for the Ti [32]. These different characteristics originate from the unique heat input/output behavior that occurs during the melting of Mg, owing to its high thermal conductivity (150 $W\cdot m^{-1}\cdot K^{-1}$) and low melting point (923 K) compared to those in Ti (thermal conductivity: 17 $W\cdot m^{-1}\cdot K^{-1}$; melting point: 1941 K) [32], as well as to the difference in process parameters (because laser scanning speed also affects the tail shape of the melt pool [48]). Consequently, spindle-shaped melt pools form in Mg alloys rather than the larger melt pools with long tails as found in Ti-based alloys, resulting in the two-dimensional growth of grains with $<11\bar{2}0>$ in the xy-plane (Fig. 3(d)).

4.2. Formation mechanism of crystallographic texture

In addition to the heat flux direction caused by single laser scanning, the direction (ex. one-way or reciprocal) and the position (ex. hatch spacing) laser scanning within one-layer are also an important factor in the development of a single-crystal-like texture of the Mg-0.5Ca alloy. Microstructural observations in the xy-plane revealed the formation of 60°-inclined microstructures with a $<11\bar{2}0>$ alignment (Fig. 6(b)), resulting in the similar development of elongated grains, as indicated by the red grains in Fig. 6(c). Fig. 9 shows a schematic of the texture formation by preferential $<11\bar{2}0>$ growth through “one-layer” reciprocal scanning. During reciprocal scanning, a fusion boundary is formed at the melt pool center (along the red or blue arrows in Fig. 9 drawn based on the observation result in Fig. 6(a)), as a result of the solidification fronts from the right and left sides of melt pool encountering upon each other. The return scanning along the red arrow melts and “overwrites” the previously solidified part in the adjacent outward scanning along blue arrow by the newly formed crystals, and vice versa. The $<11\bar{2}0>$-oriented grains develop in the outward (shown in purple) and return (shown in orange) scans grow in the parallel direction. This was achieved by the appropriate LPBF fabrication conditions employing reciprocal scanning with a hatch spacing of 0.06 mm equivalent to half the width of the melt pool. However, this cannot be achieved using unidirectional scanning (Fig. 10(a)) or an inappropriate hatch spacing (Fig. 10(b)), where the frequencies of $<11\bar{2}0>$-oriented crystal grains within 15° of the x-axis are 22.5% and 39.0%, respectively. These results suggest that crystal orientation matching between grains formed in adjacent melt pools is crucial for the formation of a strong texture.

Furthermore, most importantly, the laser scanning direction and pattern in each layer, that is, the scanning strategy, was found to be the key factor in obtaining the single-crystal-like texture of the hcp-structured materials. This was clearly demonstrated by the uneven distribution of the crystal orientation and the lower MUD values in the ±0°_SS and ±90°_SS specimens compared with the ±120°_SS specimen (Fig. 5). As shown in Fig. 9, the ±0°_SS has a possibility of the development of a single-crystal-like texture in a single layer. In reality, however, during the multiple scanning along the ±x-axis, an small ‘unsettled’ heat flux distribution occurs within the layer because the temperature increases as the laser moves along the +y-axis. Moreover, in the ±0°_SS, the unsettled distribution of the heat flux is enhanced at higher layers, resulting in the formation of a less strong crystallographic texture accompanied by $<0001>$ tilted at 30° from its original z-axis to the y-axis, as shown in Fig. 5(b). Thus, the ±0°_SS is not adequate for the formation of a strong single-crystal like texture. Likewise, the ±90°_SS resulted in a basal-fiber texture with the lowest MUD value of $<11\bar{2}0>$ among the present scanning strategies. Fig. 11 schematically explains how the features of the microstructure develop during the ±90°_SS. Considering “one-layer” as shown in Fig. 9, in the first layer of the ±90°_SS, the laser scanning along the 0° and 180°-axes tends to form a $<11\bar{2}0>$ alignment along the 0°-direction and a $<10\bar{1}0>$ alignment along the 90°-direction. In the subsequent laser scanning along the 90° and 270°-axes, however, a $<10\bar{1}0>$ alignment along the 0°-direction and a $<11\bar{2}0>$ alignment along the 90°-direction develops, as illustrated in Fig. 11. Therefore, the growths of $<11\bar{2}0>$ and $<10\bar{1}0>$ oriented grains compete with each other during the reciprocal scanning along x- and y-axes, preventing the development of a strong texture. As a result, only the basal-fiber texture with a $<0001>$ alignment along z-axis evolves.

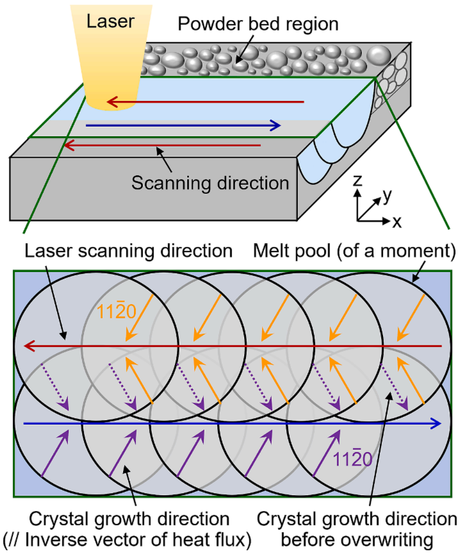

Fig. 9. Schematic of the formation of texture by preferential $<11\bar{2}0>$ growth on the “one-layer” reciprocal scanning. Overlap of the melt pool during the reciprocal scanning in each layer, which assists the crystal growth along the 60°-inclined direction about the laser scanning direction along x-axis.

In contrast to the ±0°_SS and the ±90°_SS, a single-crystal-like texture could be developed by the ±120°_SS as we expected (Fig. 5). As described in Fig. 11, in the “one-layer” reciprocal scanning, two of three $<11\bar{2}0>$ preferential alignment was achieved along the 60°-inclined directions; consequently, the remaining $<11\bar{2}0>$ direction aligned along the scanning direction. Such orderly directions of crystal growth are considered to be triggered by the heat flux direction as well as the formation of the fusion boundaries. A low interfacial energy is a key for developing the single crystal of hcp-structured Mg alloy because crystal grains that minimize the energy can readily be formed [49]. In the xy-plane observation, fusion boundaries (light blue broken lines in Fig. 6(b)) with a slight crystal misorientation were observed at the melt pool center along the laser scanning direction (0°). Similarly, fusion boundaries are formed along the 120°- and the 240°-axes. In this case, the six variations of $<11\bar{2}0>$ orientations will grow in the xy-plane such that the crystal misorientations occurred between adjacent grains are reduced to minimize the interfacial energy, leading to the formation of the single-crystal-like texture. Furthermore, because the crystals formed in scanning match the symmetry of the hcp structure, epitaxial growth occurred once the crystal orientation was determined, which enhanced the strength of the single-crystal-like texture.

4.3. Mechanical behaviors of LPBF-fabricated Mg-0.5Ca alloy with a strong texture

The present study demonstrated that the ±120°_SS specimens with a single-crystal-like texture show an anisotropic compressive deformation behavior as shown in Fig. 8(a, b). As previously reported [45–47], the compressive yield stress of a pure Mg single crystal varies with the crystal orientation as ~150 MPa // $<0001>$, ~1 MPa // $<11\bar{2}1.85>$, and ~12 MPa // $<11\bar{2}0>$ owing to the activation of non-basal slip, (0001) basal slip, and $\{10\bar{1}2\}$ twinning, respectively, which are different deformation modes. Similarly, the anisotropic stress–strain response in the present ±120°_SS specimens is suggested to be caused by the changes in the operative slip systems depending on the loading axis. Fig. 12 shows the estimated Schmid factors for the possible slip and twinning systems. The (0001)$<1\bar{2}1\bar{0}>$ basal slip is the most frequently operative slip system in Mg owing to its extremely low critical resolved

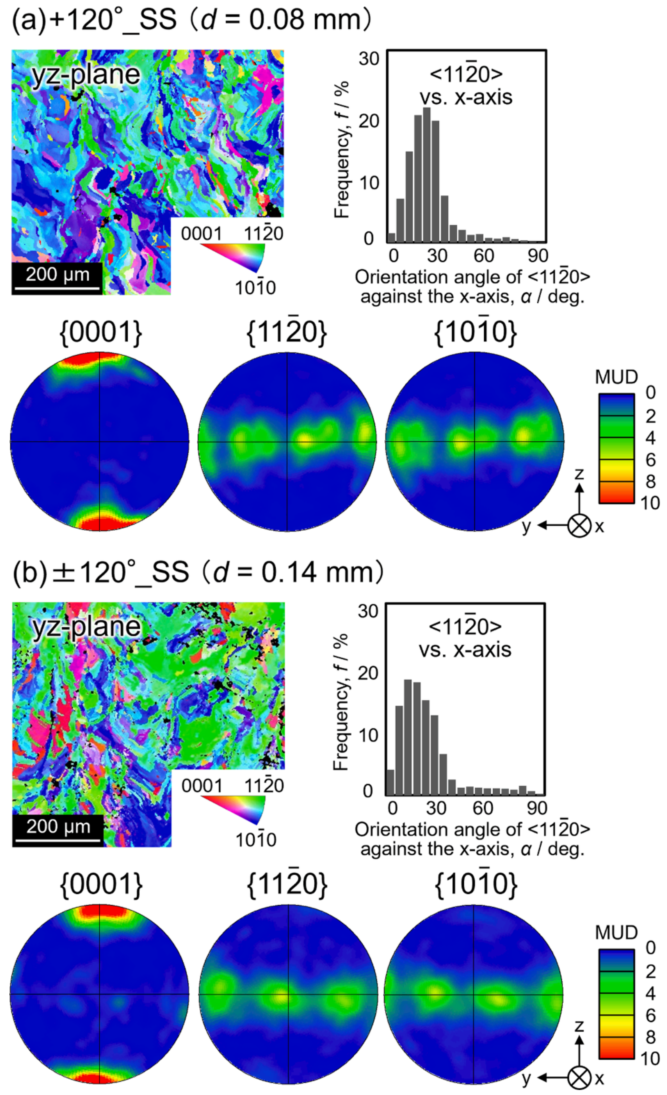

Fig. 10. Crystal orientation measured on the yz-plane, the corresponding pole figures for {0001}, {11$\bar{2}$0} and {10$\bar{1}$0}, and distribution of the orientation angle of <11$\bar{2}$0> against the x-axis, obtained from specimens fabricated by (a) the +120°_SS with 0.08 mm of hatch spacing and (b) the ±120°_SS with 0.14 mm of hatch spacing. Schematics of laser scanning passes were drawn for representing the differences of laser scanning direction (arrow direction) and hatch spacing (interval of each arrow) in both scanning strategies, compared to those in the ± 120°_SS with optimal condition. Initially written "+" and "±" of each scanning strategy mean the outward scanning and the reciprocal scanning in every layer of LPBF process, respectively.

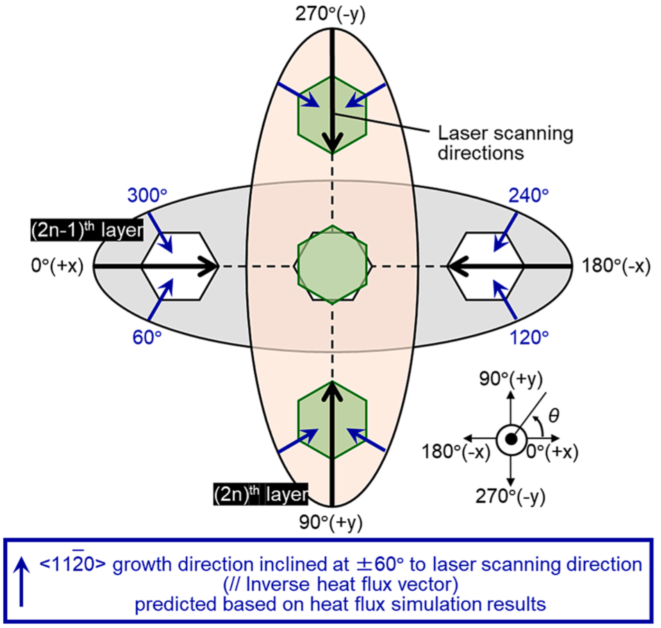

Fig. 11. Illustration of ±90°_SS showing the mismatch of crystal growth directions between reciprocal laser scanning along the 0°/180° and 90°/270°-axes, as viewed from z-axis. White and green hexagons schematically indicate the hexagonal crystal lattice developed during the laser scanning along ±x-axis and ±y-axis, respectively.

shear stress (CRSS) [45–47], and its Schmid factor is as high as ~0.43 along <11$\bar{2}$1.85> 45°(x)-axis and <$\bar{1}$101.07> 45°(y)-axis. On the other hand, the Schmid factor for basal slip was smaller than 0.25 in other loading axes. Instead, the Schmid factor for {11$\bar{2}$2}<11$\bar{2}$3> pyramidal slip is the highest when the specimen is deformed along the <0001> z-axis. Similarly, the Schmid factors for non-basal slips, namely {10$\bar{1}$0}<1$\bar{2}$10> prismatic slip and {11$\bar{2}$2}<11$\bar{2}$3> pyramidal slip, are significantly higher than that of basal slip when the specimen is deformed along the <11$\bar{2}$0> x-axis and <$\bar{1}$100> y-axis. These features are in good agreement with those expected for an ideal single crystal [46,47]. Concerning twinning, it is known that {10$\bar{1}$2}<10$\bar{1}$1> twins frequently occur over a wide range of loading directions due to its low critical resolved shear stress (CRSS) of around 5 MPa [47]. It was confirmed that the Schmid factors of {10$\bar{1}$2}<10$\bar{1}$1> twinning are smaller than 0.13 under compression along <0001> z-axis, <11$\bar{2}$1.85> 45°(x)-axis and <$\bar{1}$101.07> 45°(y)-axis. On the other hand, the values are as high as ~0.38 and ~0.42 under compression along <11$\bar{2}$0> x-axis and <$\bar{1}$100> y-axis, respectively. These variations are also in good agreement with those in ideal Mg single crystals, whose values are ~0.37 compressed along the <11$\bar{2}$0> and ~0.50 compressed along the <$\bar{1}$100> [47,50]. Based on the above considerations, it is suggested that {0001}<11$\bar{2}$0> basal slip is activated under compression along <11$\bar{2}$1.85> 45°(x)-axis and <$\bar{1}$101.07> 45°(y)-axis, whereas {11$\bar{2}$2}<11$\bar{2}$3> pyramidal slip is activated along <0001> z-axis, and {10$\bar{1}$2}<10$\bar{1}$1> twinning is activated under compression along <11$\bar{2}$0> x-axis and <$\bar{1}$100> y-axis.

The activation of {10$\bar{1}$2}<10$\bar{1}$1> twinning was indeed confirmed by the deformed microstructure characterization. Fig. 12(b) shows a crystal orientation map obtained in the specimen compressed along the <$\bar{1}$100> y-axis. Since the inspected surface of the specimen is perpendicular to the z-axis, the crystal orientation is predominantly near <0001>, i.e. shown in red. However, many lenticular grains (appearing in blue) are observed after deformation. As shown in Fig. 12(c), the misorientation angle between the matrix and the lenticular grains is approximately 86°, indicating that these are {10$\bar{1}$2}<10$\bar{1}$1> twins formed during the compression test.

The "order" of yield stress magnitudes was consistent with that of specimens prepared from the single crystal and the ±120°_SS specimen; [0001] > [11$\bar{2}$0] ≅ [$\bar{1}$100] > [$\bar{1}$101.07] ≅ [11$\bar{2}$1.85]. The similarity of the stress-strain curves of <$\bar{1}$101.07> and <11$\bar{2}$1.85>, and of<$\bar{1}$100> and <11$\bar{2}$0> is explained by the comparable Schmid factors. However, compared to the deformation behavior of the Mg single crystals, the ±120°_SS specimens showed comparable yield stress along the <0001> z-axis, but exhibited much higher yield stress along the <11$\bar{2}$0> x-axis, <$\bar{1}$100> y-axis, <11$\bar{2}$1.85> 45°(x)-axis, and <$\bar{1}$101.07> 45°(y)-axis. This can be attributed to i) the introduction of large numbers of dislocation cells (Fig. 6(e)) and grain boundaries (Fig. 5(a)), ii) precipitation hardening with fine Ca-containing particles (Fig. 6(f)), and iii) solid solution strengthening due to the excess concentration (0.2 wt.%) of Ca etc., in the ±120°_SS specimens. Further

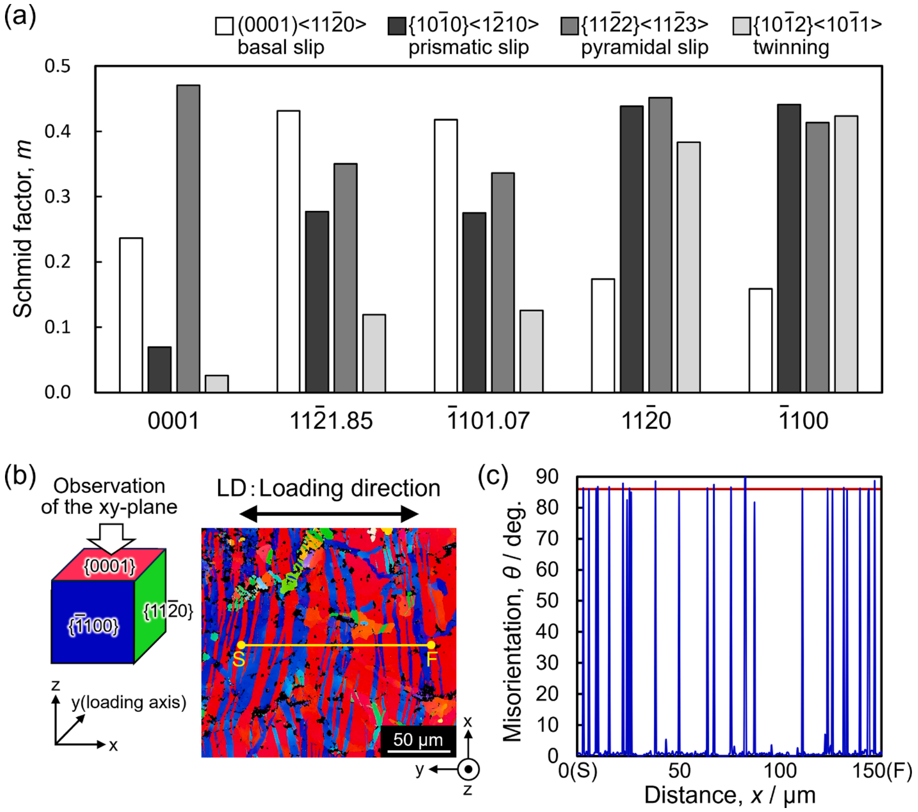

Fig. 12. Estimation of deformation modes in the ±120°_SS specimens at each loading axis. (a) Schmid factors for possible slip and twinning systems. (b) Crystal orientation map measured on the xy-plane of the specimen compressed to a plastic stain of 2% along the <$\bar{1}$100> y-axis. (c) The misorientation between neighboring pixels from S to F in (b). The red line at 86.3° is the characteristic misorientation associated with {10$\bar{1}$2}<10$\bar{1}$1> twinning.

studies are required to precisely and quantitatively evaluate the contribution of those factors.

5. Conclusion and outlook

This study is the first to establish a design principle for how to optimize LPBF scanning strategies that enable the formation of single-crystal-like textures in hcp-structured materials. It demonstrates pronounced mechanical anisotropy related to the strong texture in a hcp-structured Mg alloy manufactured using LPBF. The conclusions are summarized as follows.

i. A novel scanning strategy, termed "±120°_SS" was designed based on heat flux analysis and the six-fold rotational symmetry along the [0001] axis inherent to the hcp structure.
ii. By applying the "±120°_SS" scanning strategy to the Mg-0.5Ca alloy, a single-crystal-like texture was successfully formed, characterized by a <0001> orientation along the building direction (z-axis) and <11$\bar{2}$0> orientations along the 0° (x-axis), 120°, and 240° directions. This demonstrates that the laser scanning strategy can precisely control crystal growth, enabling intentional formation of an extremely strong texture even in a hcp-structured material.
iii. The strongly textured Mg-0.5Ca alloy specimens exhibited anisotropy in compressive mechanical properties depending on the loading axis, similar to those observed in Mg-single crystals. The yield stress differed by 2.7 times when comparing loading along the <0001> axis and the <$\bar{1}$101.07> axis.

We believe the proposed design principle for optimization of scanning strategies is not limited to hcp-structured Mg alloys; it is also applicable to other materials with low crystallographic symmetry. The work thus represents a significant advancement in the control of crystallographic texture in additive manufacturing.

CRediT authorship contribution statement

Ryosuke Ozasa: Writing – review & editing, Writing – original draft, Software, Methodology, Investigation, Formal analysis, Data curation, Conceptualization. **Yuta Kizawa:** Software, Methodology, Investigation, Formal analysis. **Kakeru Okawa:** Methodology, Investigation, Formal analysis. **Koji Hagihara:** Writing – review & editing, Validation, Supervision. **Kazuhisa Sato:** Methodology, Formal analysis. **Toshiharu Matsumoto:** Methodology, Investigation. **Toko Tokunaga:** Methodology, Investigation, Formal analysis. **Naoko Ikeo:** Methodology, Investigation. **Viritpon Srimaneepong:** Methodology, Investigation. **Pan Wang:** Writing – review & editing, Validation. **Dorte Juul Jensen:** Writing – original draft, Validation, Funding acquisition. **Takayoshi Nakano:** Writing – review & editing, Validation, Supervision, Project administration, Funding acquisition, Conceptualization.

Funding

This work was partly supported by CREST-Nanomechanics: Elucidation of Macroscale Mechanical Properties Based on Understanding Nanoscale Dynamics for Innovative Mechanical Materials (Grant No. JPMJCR2194) from the Japan Science and Technology Agency (JST), Grants-in-Aid for Scientific Research (Grant No. 22H01812, 23H00235 and 25K00051) from the Japan Society for the Promotion of Science (JSPS), and VILLUM FONDEN (Grant No. VIL54495).

Declaration of competing interest

The authors declare that they have no known competing financial interests or personal relationships that could have appeared to influence the work reported in this paper.

Acknowledgments

A part of this work was supported by ARIM Project of the Ministry of Education, Culture, Sports, Science and Technology, Japan (MEXT), Grant No. JPMXP1223OS0043 at the Research Center for UHVEM (Nanotechnology Open Facilities) in The University of Osaka. The authors thank Mr. K. Kimura for his help with operation of LPBF machine and Dr. S. Takagi for his help with FIB microsampling.

Role of the funding source

The funders played no role in the study design, data collection, data analysis, data interpretation, or writing of the reports.

Data availability

Data will be made available on request.

References

[1] Z. Xia, Y. Kang, Q. Wang, Developments in the production of grain-oriented electrical steel, J. Magn. Magn. Mater. 320 (2008) 3229–3233, https://doi.org/10.1016/j.jmmm.2008.07.003.

[2] S. Higashino, D. Miyashita, T. Ishimoto, E. Miyoshi, T. Nakano, M. Tane, Low Young's modulus in laser powder bed fusion processed Ti–15Mo–5Zr–3Al alloys achieved by the control of crystallographic texture combined with the retention of low-stability bcc structure, Addit. Manuf. 102 (2025) 104720, https://doi.org/10.1016/j.addma.2025.104720.

[3] W. Xia, X. Zhao, L. Yue, Z.e. Zhang, A review of composition evolution in Ni-based single crystal superalloys, J. Mater. Sci. Technol. 44 (2020) 76–95, https://doi.org/10.1016/j.jmst.2020.01.026.

[4] S. Graff, W. Brocks, D. Steglich, Yielding of magnesium: From single crystal to polycrystalline aggregates, Int. J. Plast. 23 (2007) 1957–1978, https://doi.org/10.1016/j.ijplas.2007.07.009.

[5] K. Hagihara, M. Okubo, M. Yamasaki, T. Nakano, Crystal-orientation-dependent corrosion behaviour of single crystals of a pure Mg and Mg-Al and Mg-Cu solid solutions, Corros. Sci. 109 (2016) 68–85, https://doi.org/10.1016/j.corsci.2016.03.019.

[6] M. Tane, Y. Nagai, H. Kimizuka, K. Hagihara, Y. Kawamura, Elastic properties of an Mg-Zn-Y alloy single crystal with a long-period stacking-ordered structure, Acta Mater. 61 (2013) 6338–6351, https://doi.org/10.1016/j.actamat.2013.06.041.

[7] J. Bočan, J. Maňák, A. Jäger, Anisotropic mechanical properties of pure magnesium analyzed by in situ nanoindentation, Key Eng. Mat. 662 (2015) 11–14, https://doi.org/10.4028/www.scientific.net/KEM.662.11.

[8] X. Huang, K. Suzuki, Y. Chino, M. Mabuchi, Texture and stretch formability of AZ61 and AM60 magnesium alloy sheets processed by high-temperature rolling, J. Alloys Compd. 632 (2015) 94–102, https://doi.org/10.1016/j.jallcom.2015.01.148.

[9] L. Tian, L. Wang, H. Wu, H. Wang, L. Zheng, K.S. Shin, Recent research advances in Mg single crystal based on the crystal orientations: A review, J. Mater. Res. Technol. 27 (2023) 5572–5593, https://doi.org/10.1016/j.jmrt.2023.10.273.

[10] N. Ikeo, H. Fukuda, A. Matsugaki, T. Inoue, A. Serizawa, T. Matsuzaka, T. Ishimoto, R. Ozasa, O. Gokcekaya, T. Nakano, 3D puzzle in cube pattern for anisotropic/isotropic mechanical control of structure fabricated by metal additive manufacturing, Crystals 11 (2021) 959, https://doi.org/10.3390/cryst11080959.

[11] T. Ishimoto, R. Ozasa, K. Nakano, M. Weinmann, C. Schnitter, M. Stenzel, A. Matsugaki, T. Nagase, T. Matsuzaka, M. Todai, H.S. Kim, T. Nakano, Development of TiNbTaZrMo bio-high entropy alloy (BioHEA) super-solid solution by selective laser melting, and its improved mechanical property and biocompatibility, Scr. Mater. 194 (2021) 113658, https://doi.org/10.1016/j.scriptamat.2020.113658.

[12] O. Gokcekaya, T. Ishimoto, Y. Nishikawa, Y.S. Kim, A. Matsugaki, R. Ozasa, M. Weinmann, C. Schnitter, M. Stenzel, H.S. Kim, Y. Miyabayashi, T. Nakano, Novel single-crystal-like non-equiatomic TiZrHfNbTaMo bio-high entropy alloy (BioHEA) developed by laser powder bed fusion, Mater. Res. Lett. 11 (2023) 274–280, https://doi.org/10.1080/21663831.2022.2147406.

[13] H. Amano, T. Ishimoto, R. Suganuma, K. Aiba, S.-H. Sun, R. Ozasa, T. Nakano, Effect of a helium gas atmosphere on the mechanical properties of Ti-6Al-4V Alloy built with laser powder bed fusion: a comparative study with argon gas, Addit. Manuf. 48 (2021) 102444, https://doi.org/10.1016/j.addma.2021.102444.

[14] T. Ishimoto, K. Hagihara, K. Hisamoto, S.-H. Sun, T. Nakano, Crystallographic texture control of beta-type Ti-15Mo-5Zr-3Al alloy by selective laser melting for the development of novel implants with a biocompatible low Young's modulus, Scr. Mater. 132 (2017) 34–38, https://doi.org/10.1016/j.scriptamat.2016.12.038.

[15] K. Hagihara, T. Nakano, Control of anisotropic crystallographic texture in powder bed fusion additive manufacturing of metals and ceramics - a review, J. Met. 74 (2022) 1760–1773, https://doi.org/10.1007/s11837-021-04966-7.

[16] T. Mukherjee, J.W. Elmer, H.L. Wei, T.J. Lienert, W. Zhang, S. Kou, T. DebRoy, Control of grain structure, phases, and defects in additive manufacturing of high-performance metallic components, Prog. Mater. Sci. 138 (2023) 101153, https://doi.org/10.1016/j.pmatsci.2023.101153.

[17] Xu. Wenhe, J. Li, Z. Zhang, H. Yuan, G. An, H. Shi, C. Cai, W. Jiang, W. Li, Q. Wei, Laser powder bed fusion of WE43 magnesium alloy with superior balance of strength and ductility, J. Magnes. Alloys 13 (2025) 1275–1293, https://doi.org/10.1016/j.jma.2024.03.012.

[18] W. Chen, B. Yin, K. Li, R. Liao, B. Li, H. Huang, Wu. Yingjie, P. Wen, B. Jiang, F. Pan, Superstrengthening effect of beyond-solid-solution laser powder bed fused WE43 magnesium alloy triggered by direct aging treatment, Addit. Manuf. 89 (2024) 104287, https://doi.org/10.1016/j.addma.2024.104287.

[19] C. Ji, L. Zhu, B. Yin, S. Bai, L.E. Murr, P. Wen, B. Jiang, F. Pan, K. Li, Temperature-dependent mechanical behaviors of laser powder bed fused WE43 alloy with heterogeneous grain structure: Deformation and fracture mechanisms, J. Alloys Compd. 1033 (2025) 181288, https://doi.org/10.1016/j.jallcom.2025.181288.

[20] C. Ji, K. Li, R. Liao, Z. Li, B. Yin, P. Wen, B. Jiang, L.E. Murr, F. Pan, Tensile creep mechanisms of laser powder bed fused WE43 alloy with heterogeneous microstructure: Evolution in dislocations and precipitates, J. Mater. Sci. Technol. 238 (2025) 209–229, https://doi.org/10.1016/j.jmst.2025.02.063.

[21] X. Li, X. Fang, X. Jiang, Y. Duan, Y. Li, H. Zhang, X. Li, K.e. Huang, Additively manufactured high-performance AZ91D magnesium alloys with excellent strength and ductility via nanoparticles reinforcement, Addit. Manuf. 69 (2023) 103550, https://doi.org/10.1016/j.addma.2023.103550.

[22] Q. Deng, Wu. Yujuan, Y. Luo, Su. Ning, X. Xue, Z. Chang, Wu. Qianye, Y. Xue, L. Peng, Fabrication of high-strength Mg-Gd-Zn-Zr alloy via selective laser melting, Mater. Charact. 165 (2020) 110377, https://doi.org/10.1016/j.matchar.2020.110377.

[23] N.A. Zumdick, L. Jauer, L.C. Kersting, T.N. Kutz, J.H. Schleifenbaum, D. Zander, Additive manufactured WE43 magnesium: A comparative study of the microstructure and mechanical properties with those of powder extruded and as-cast WE43, Mater. Charact. 147 (2019) 384–397, https://doi.org/10.1016/j.matchar.2018.11.011.

[24] Y. Wan, G. Xiong, H. Luo, F. He, Y. Huang, X. Zhou, Preparation and characterization of a new biomedical magnesium–calcium alloy, Mater. Des. 29 (2008) 2034–2037, https://doi.org/10.1016/j.matdes.2008.04.017.

[25] P. Makkar, S.K. Sarkar, A.R. Padalhin, B.-G. Moon, Y.S. Lee, B.T. Lee, In vitro and in vivo assessment of biomedical Mg-Ca alloys for bone implant applications, J. Appl. Biomater. Funct. Mater. 16 (2018) 126–136, https://doi.org/10.1177/2280800017750359.

[26] X. Jing, F. Wang, L. Tian, G. Hou, J. She, A. Tang, The design strategy for developing low-alloyed Mg-Ca alloy with excellent mechanical properties and ignition resistance, J. Alloys Compd. 1044 (2025) 184357, https://doi.org/10.1016/j.jallcom.2025.184357.

[27] S.-H. Ha, J.-K. Lee, H.-H. Jo, S.-B. Jung, S.K. Kim, Behavior of CaO and calcium in pure magnesium, Rare Met. 25 (2006) 150–154, https://doi.org/10.1016/S1001-0521(08)60071-6.

[28] C.J. Todaro, M.A. Easton, D. Qiu, M. Brandt, D.H. StJohn, M. Qian, Grain refinement of stainless steel in ultrasound-assisted additive manufacturing, Addit. Manuf. 37 (2021) 101632, https://doi.org/10.1016/j.addma.2020.101632.

[29] A. Chapuis, J.H. Driver, Temperature dependency of slip and twinning in plane strain compressed magnesium single crystals, Acta Mater. 59 (2011) 1986–1994, https://doi.org/10.1016/j.actamat.2010.11.064.

[30] S. Nimityongskul, M. Jones, H. Choi, R. Lakes, S. Kou, X. Li, Grain refining mechanisms in Mg–Al alloys with Al_4C_3 microparticles, Mater. Sci. Eng., A 527 (2010) 2104–2111, https://doi.org/10.1016/j.msea.2009.12.030.

[31] S. Ganeshan, S.L. Shang, Y. Wang, Z.-K. Liu, Effect of alloying elements on the elastic properties of Mg from first-principles calculations, Acta Mater. 57 (2009) 3876–3884, https://doi.org/10.1016/j.actamat.2009.04.038.

[32] T. Todo, T. Ishimoto, O. Gokcekaya, J. Oh, T. Nakano, Single-crystal-like crystallographic texture formation of pure tungsten through laser powder bed fusion, Scr. Mater. 206 (2022) 114252, https://doi.org/10.1016/j.scriptamat.2021.114252.

[33] A. Takase, T. Ishimoto, N. Morita, N. Ikeo, T. Nakano, Comparison of phase characteristics and residual stresses in Ti-6Al-4V alloy manufactured by laser powder bed fusion (L-PBF) and electron beam powder bed fusion (EB-PBF) techniques, Crystals 11 (2021) 796, https://doi.org/10.3390/cryst11070796.

[34] Q. Chen, X. Liang, D. Hayduke, J. Liu, L. Cheng, J. Oskin, R. Whitmore, A.C. To, An inherent strain based multiscale modeling framework for simulating part-scale residual deformation for direct metal laser sintering, Addit. Manuf. 28 (2019) 406–418, https://doi.org/10.1016/j.addma.2019.05.021.

[35] M.-S. Pham, B. Dovgyy, P.A. Hooper, C.M. Gourlay, A. Piglione, The role of side-branching in microstructure development in laser powder-bed fusion, Nat. Commun. 11 (2020) 749, https://doi.org/10.1038/s41467-020-14453-3.

[36] H.J. Willy, X. Li, Z. Chen, T.S. Herng, S. Chang, C.Y.A. Ong, C. Li, J. Ding, Model of laser energy absorption adjusted to optical measurements with effective use in finite element simulation of selective laser melting, Mater. Des. 157 (2018) 24–34, https://doi.org/10.1016/j.matdes.2018.07.029.

[37] G.L. Knapp, N. Raghavan, A. Plotkowski, T. DebRoy, Experiments and simulations on solidification microstructure for Inconel 718 in powder bed fusion electron

beam additive manufacturing, Addit. Manuf. 25 (2019) 511–521, https://doi.org/10.1016/j.addma.2018.12.001.

[38] S. Liu, H. Zhu, G. Peng, J. Yin, X. Zeng, Microstructure prediction of selective laser melting AlSi10Mg using finite element analysis, Mater. Des. 142 (2018) 319–328, https://doi.org/10.1016/j.matdes.2018.01.022.

[39] B. Al Mangour, J. Cheng, D. Grzesiak, Y.J. Hwang, K.A. Lee, Fundamental study on the development of pure magnesium parts by additive manufacturing: An experimental and computational analysis, Met. Mater. Int. 29 (2023) 429–443, https://doi.org/10.1007/s12540-022-01300-x.

[40] N. Raghavan, R. Dehoff, S. Pannala, S. Simunovic, M. Kirka, J. Turner, N. Carlson, S.S. Babu, B.A. Mangour, J. Cheng, D. Grzesiak, Y.J. Hwang, K.A. Lee, Numerical modeling of heat-transfer and the influence of process parameters on tailoring the grain morphology of IN718 in electron beam additive manufacturing, Acta Mater. 112 (2016) 303–314, https://doi.org/10.1016/j.actamat.2016.03.063.

[41] M. Paliwal, I.H. Jung, The evolution of the growth morphology in Mg-Al alloys depending on the cooling rate during solidification, Acta Mater. 61 (2013) 4848–4860, https://doi.org/10.1016/j.actamat.2013.04.063.

[42] J. Du, Z. Guo, A. Zhang, M. Yang, M. Li, S. Xiong, Correlation between crystallographic anisotropy and dendritic orientation selection of binary magnesium alloys, Sci. Rep. 7 (2017) 13600, https://doi.org/10.1038/s41598-017-12814-5.

[43] M. Esmaily, Z. Zeng, A.N. Mortazavi, A. Gullino, S. Choudhary, T. Derra, F. Benn, F. D'Elia, M. Müther, S. Thomas, A. Huang, A. Allanore, A. Kopp, N. Birbilis, A detailed microstructural and corrosion analysis of magnesium alloy WE43 manufactured by selective laser melting, Addit. Manuf. 35 (2020) 101321, https://doi.org/10.1016/j.addma.2020.101321.

[44] T.B. Massalski, H. Okamoto (Eds.), Binary Alloy Phase Diagrams, ASM International, Materials Park, OH, 1990, p. 927.

[45] S. Ando, M. Tsushida, H. Kitahara, Deformation behavior of magnesium single crystal in *c*-axis compression and *a*-axis tension, Mater. Sci. Forum 654–656 (2010) 699–702, https://doi.org/10.4028/www.scientific.net/MSF.654-656.699.

[46] A. Chapuis, J.H. Driver, Temperature dependency of slip and twinning in plane strain compressed magnesium single crystals, Acta Mater. 59 (2011) 1986–1994, https://doi.org/10.1016/j.actamat.2010.11.064.

[47] K. Hagihara, R. Ueyama, M. Yamasaki, Y. Kawamura, T. Nakano, Surprising increase in yield stress of Mg single crystal using long-period stacking ordered nanoplates, Acta Mater. 209 (2021) 116797, https://doi.org/10.1016/j.actamat.2021.116797.

[48] J. Wang, R. Zhu, Y. Liu, L. Zhang, Understanding melt pool characteristics in laser powder bed fusion: An overview of single- and multi-track melt pools for process optimization, Adv. Powder Mater. 2 (2023) 100137, https://doi.org/10.1016/j.apmate.2023.100137.

[49] T. Ishimoto, N. Morita, R. Ozasa, A. Matsugaki, O. Gokcekaya, S. Higashino, M. Tane, T. Mayama, K. Cho, H.Y. Yasuda, M. Okugawa, Y. Koizumi, M. Yoshiya, D. Egusa, T. Sasaki, E. Abe, H. Kimizuka, N. Ikeo, T. Nakano, Superimpositional design of crystallographic textures and macroscopic shapes via metal additive manufacturing–Game-change in component design, Acta Mater. 286 (2025) 120709, https://doi.org/10.1016/j.actamat.2025.120709.

[50] K. Hagihara, M. Sugita, M. Yamasaki, T. Tokunaga, T. Mayama, S. Nishimoto, Unique orientation dependence of mechanical properties of Mg/LPSO extruded alloys, J. Alloys Compd. 1061 (2026) 187197, https://doi.org/10.1016/j.jallcom.2026.187197.